

Highlights

Can spinodal decomposition occur during decompression-induced vesiculation of magma?

Mizuki Nishiwaki

- Magma vesiculation during decompression was interpreted by simple thermodynamics.
- Binodal and spinodal curves of silicate–water systems were drawn versus pressure.
- Magma vesiculation probably occurs by nucleation, not by spinodal decomposition.
- Spinodal pressure can contribute to an easy estimate of bubble surface tension.

Can spinodal decomposition occur during decompression-induced vesiculation of magma?

Mizuki Nishiwaki^a

^a*Center for Glass Science & Technology, School of Engineering, The University of Shiga Prefecture, 2500, Hassaka-cho, Hikone, Shiga, 522-8533, Japan*

Abstract

Volcanic eruptions are driven by decompression-induced vesiculation of supersaturated volatile components in magma. The initial phase of this phenomenon has long been described as a process of nucleation and growth. Recently, it was proposed that spinodal decomposition (an energetically spontaneous phase separation that does not require the formation of a distinct interface) may occur during decompression-induced magma vesiculation. This suggestion has attracted considerable attention, but is currently only based on textural observations of decompression experiment products (the independence of bubble number density on decompression rate; the homogeneous spatial distribution of the bubbles). In this study, I used a simple thermodynamic approach to investigate whether spinodal decomposition can occur during the decompression-induced vesiculation of magma. I drew the binodal and spinodal curves on the chemical composition–pressure plane by approximating hydrous magmas at several conditions of temperature and chemical composition as two-component symmetric regular solutions of silicate and water, and using experimentally

determined values of water solubility in these magmas. The spinodal curve was much lower than the binodal curve for all the magmas at pressures sufficiently below the second critical endpoint. In addition, the final pressure of all the decompression experiments performed to date fell between these two curves. This suggests that spinodal decomposition is unlikely to occur in the pressure range of magmatic processes in the continental crust, and that decompression-induced magma vesiculation results from nucleation and subsequent growth, as previously considered. In addition, it is expected that by substituting the determined spinodal pressure into the formula of non-classical nucleation theory, the surface tension between the silicate melt and bubble nucleus can be easily estimated.

Keywords: hydrous magma, vesiculation, nucleation, spinodal decomposition, thermodynamics, regular solution

1. Introduction

Magma degassing is one of the strongest controlling factors in the dynamics of volcanic eruptions. Volatiles (e.g., H_2O , CO_2 , H_2S) initially dissolved in magma deep underground become insoluble under decompression, precipitating as vapor (bubbles). Understanding this magma vesiculation process is crucial because it dramatically influences eruption style and volcanic explosivity, playing a key role in determining the time evolution of eruptions, ranging from effusive lava flows to highly explosive pyroclastic events. In particular, water often makes up a large

proportion of the various volatile components, and its degassing—in a
 precise sense, the phase separation into silicate melt saturated with water
 and supercritical water vapor saturated with trace amounts of silicate—has
 been extensively studied since Verhoogen (1951). The initial degassing
 stage has long been understood as nucleation and growth (e.g., Shimozuru
 et al., 1957; Murase and McBirney, 1973; Sparks, 1978), and theoretical
 numerical models were constructed by Toramaru (1989, 1995) to predict
 the bubble number density (BND) based on classical nucleation theory
 (CNT, e.g., Hirth et al., 1970). In addition, in the last 30 years since
 the innovative work by Hurwitz and Navon (1994), many experiments
 have been conducted to reproduce decompression-induced vesiculation of
 mainly water-dissolved (hydrous) magmas in laboratory experimental magma
 analogues with controlled decompression rates. As data from decompression
 experiments to date generally agreed with numerical predictions (BND
 $\propto |\text{decompression rate}|^{1.5}$ by Toramaru, 1995) based on CNT, Toramaru
 (2006) constructed the BND decompression rate meter (BND decompression
 rate meter). This equation is approximately valid for both homogeneous
 nucleation of spherical bubbles in a uniform melt (where σ is large) and
 heterogeneous nucleation of bubbles on crystal surfaces such as Fe–Ti oxides
 (where σ is small) by applying appropriate corrections to the surface tension
 σ between the melt and bubble nucleus (Shea, 2017; Toramaru, 2022).
 This theoretical model has been used extensively to estimate magma’s
 decompression rate in a volcanic conduit based on quantitative analysis

of bubble texture in natural pyroclastic products (e.g., Toramaru, 2006; 33
Giachetti et al., 2010; Houghton et al., 2010; Nguyen et al., 2014). 34

However, some laboratory experiments performed thus far have reported 35
results that are anharmonic to the above equations; Allabar and Nowak 36
(2018) performed decompression experiments on hydrous phonolitic melts 37
over a wide range of decompression rates, including 0.024–1.7 MPa/s, 38
and found systematically high BND values (5.2 mm^{-3}) independent of 39
decompression rate. To explain this result, they proposed a scenario 40
in which spinodal decomposition, rather than nucleation as used in 41
previous explanations, occurs in the early stages of decompression-induced 42
vesiculation. Spinodal decomposition is the phase separation of a 43
multi-component mixture or solid solution due to energetic instability (e.g., 44
Cahn and Hilliard, 1959; Cahn, 1965). When the system’s temperature, 45
pressure, and chemical composition (T, P, X) are within the miscibility 46
gap, whether nucleation or spinodal decomposition occurs is determined 47
by the sign of the second-order derivative of the system’s molar Gibbs 48
energy of mixing g^{real} . If the sign is positive, the system is metastable, 49
and nucleation occurs, with distinct phase boundaries (interfaces) appearing 50
spatially random from the beginning. Conversely, if the sign is negative, 51
the system becomes unstable, and spinodal decomposition occurs, in which 52
initially small concentration fluctuations with an unclear phase boundary 53
gradually grow and eventually lead to the separation of two phases at a 54
specific wavelength, forming a distinct interface. The diffusion coefficient is 55

proportional to the second-order derivative of g^{real} , so nucleation corresponds
 to downhill diffusion, where diffusion progresses in the direction that weakens
 the concentration gradient. In contrast, spinodal decomposition corresponds
 to uphill diffusion, where diffusion progresses in the direction that strengthens
 the concentration gradient (Haasen, 1996). In Allabar and Nowak (2018),
 spinodal decomposition was proposed for two reasons: (1) the timescale
 for spinodal decomposition in gas–liquid systems is much shorter than the
 timescale for decompression (Debenedetti, 2000), which could explain the
 absence of dependence on BND on the decompression rate. (2) The bubble
 spatial distribution in the experimental products was homogeneous; the
 vitrified silicate melt and bubbles appeared to phase-separate at a specific
 wavelength. Subsequent work by Sahagian and Carley (2020) raised the
 problem that “the surface tension between the melt and tiny bubble nucleus
 should act to push dissolved volatiles back into the melt, but bubbles of
 such size are still formed” and discussed this process as the “tiny bubble
 paradox.” They extended the ideas of Allabar and Nowak (2018) as follows:
 if spinodal decomposition—rather than nucleation—occurs, this paradox can
 be resolved because interface formation is no longer necessary and explains
 the homogeneous spatial distribution of bubbles observed in some laboratory
 products.

Thus, the new theory that “decompression-induced vesiculation of magma
 can occur not only by nucleation but also by spinodal decomposition”
 has been actively discussed and has attracted much attention in the last

seven years. Gardner et al. (2023) also stated that future interpretations
of BND and bubble size distributions of natural volcanic products must
consider the possibility that various mechanisms of bubble formation may
occur, including nucleation (homogeneous and heterogeneous) and spinodal
decomposition. However, whether spinodal decomposition actually occurs
during decompression-induced magma vesiculation remains speculative.
Nonetheless, owing to the small spatiotemporal scale of the physical
phenomena under investigation, it is likely to be extremely difficult to
confirm via laboratory observational experiments. Therefore, in this paper,
I discuss which nucleation or spinodal decomposition mechanism is likely to
occur during decompression-induced magma vesiculation, based on a simple
thermodynamic approach.

This study first reviews the thermodynamic definitions of nucleation and
spinodal decomposition. Spinodal decomposition, which has traditionally
been treated when it occurs with a change in temperature at constant
pressure, can also be treated with a change in pressure at constant
temperature. An attempt is made to consider hydrous magmas in a
simplified way as a symmetric regular solution of silicate and water
and to draw binodal and spinodal curves quantitatively on the chemical
composition–pressure plane using a simple calculation. Next, based on
the calculation results, I discussed the possibility of spinodal decomposition
occurring in decompressing magma. Furthermore, I provided insights on the
kinetic effects that should be considered in real systems and how the results

of previous decompression experiments should be interpreted about the BND
decompression rate meter. Finally, as a potential application of the model
proposed in this study, an estimate of the surface tension between the melt
and the bubble nucleus was presented.

2. Energetics on the mixing of silicate and water

2.1. General theory: Thermodynamic energetics of two-component mixture

Notations used in this study are listed in Table 1. Here, I will explain the
thermodynamics of a two-component mixture. In general, the molar Gibbs
energy of a mixture, g^{real} , is described as the sum of the ideal solution's
Gibbs energy, g^{ideal} (which arises from configurational entropy), and the
excess energy, g^{excess} ($\neq 0$, represents the deviation from the ideal solution)
(e.g., Guggenheim, 1952):

$$g^{\text{real}} = g^{\text{ideal}} + g^{\text{excess}}, \quad (1)$$

where the amount obtained by proportionally distributing and summing the
Gibbs energies of each pure phase is subtracted as the baseline. In an ideal
solution, $g^{\text{excess}} = 0$. Several types of non-ideal solutions that take into
account the deviation from the ideal solution, $g^{\text{excess}} \neq 0$; among them, the
most basic type is the regular solution. In a regular solution, the non-ideal
entropy is neglected ($s^{\text{excess}} = 0$), and the non-ideal enthalpy is treated as
 $h^{\text{excess}} \neq 0$, which leads to the relationship $g^{\text{excess}} = h^{\text{excess}}$. Here, x represents

the mole fraction of one of the components ($0 < x < 1$). In this case, as
explained below, g^{ideal} is always symmetric with respect to $x = 0.5$, while the
shape of g^{excess} (and g^{real}) is assumed to be either symmetric or asymmetric.
The g^{ideal} at a given temperature T is expressed by the following equation.

$$g^{\text{ideal}} = RT\{x \ln x + (1 - x) \ln(1 - x)\}. \quad (2)$$

The equation for g^{excess} differs depending on whether the symmetric or
asymmetric model. In the case of the symmetric model,

$$g^{\text{excess}} = x(1 - x)w_{\text{sym}}, \quad (3)$$

where w_{sym} is the interaction parameter between the two components A and
B, representing the non-ideality of mixing. In the case of the asymmetric
model,

$$g^{\text{excess}} = x(1 - x)\{w_A(1 - x) + w_Bx\}, \quad (4)$$

where w_A and w_B are the interaction parameters when a particle of A enters a
group of B, and when a particle of B enters a group of A, respectively. These
represent the slopes of the g^{excess} curve at the endpoints on the B side and A
side, where a positive slope indicates that the system becomes energetically
unstable after mixing. In contrast, a negative slope indicates that the system
becomes energetically stable. Based on this, the Gibbs energy curves for
both the symmetric and asymmetric models are illustrated as shown in Fig.

1. Here, we assume that for the symmetric model, $w_{\text{sym}} > 0$, and for the asymmetric model, $w_{\text{A}} > 0$ and $w_{\text{B}} > 0$.

The g^{real} curve for the symmetric model and its corresponding phase diagram are shown in Fig. 2. Hereafter, we focus on conditions under which the system's temperature, pressure, and chemical composition (T, P, X) lie within the miscibility gap. Compositions outside the two local minima of the g^{real} curve correspond to a single-phase system, while compositions inside these minima undergo phase separation into a two-phase system. In other words, the point where the first derivative of the g^{real} curve with respect to x equals zero corresponds to the one-phase/two-phase boundary in the phase diagram (i.e., the binodal curve). In the region between the local minimum and the inflection point, where the g^{real} curve is convex downwards (i.e., where the second-order derivative with respect to x is positive), the system is metastable, and nucleation occurs with distinct phase boundaries (interfaces) appearing randomly in space. Conversely, in the interval where the g^{real} curve is convex upward, i.e., where the sign of the second-order derivative with x is negative, the system is unstable, and spinodal decomposition occurs wherein the two phases start to separate at a specific wavelength with unclear phase boundaries. In other words, the point where the second derivative of the g^{real} curve with respect to x equals 0 corresponds to the nucleation/spinodal decomposition boundary (i.e., the spinodal curve) in the phase diagram.

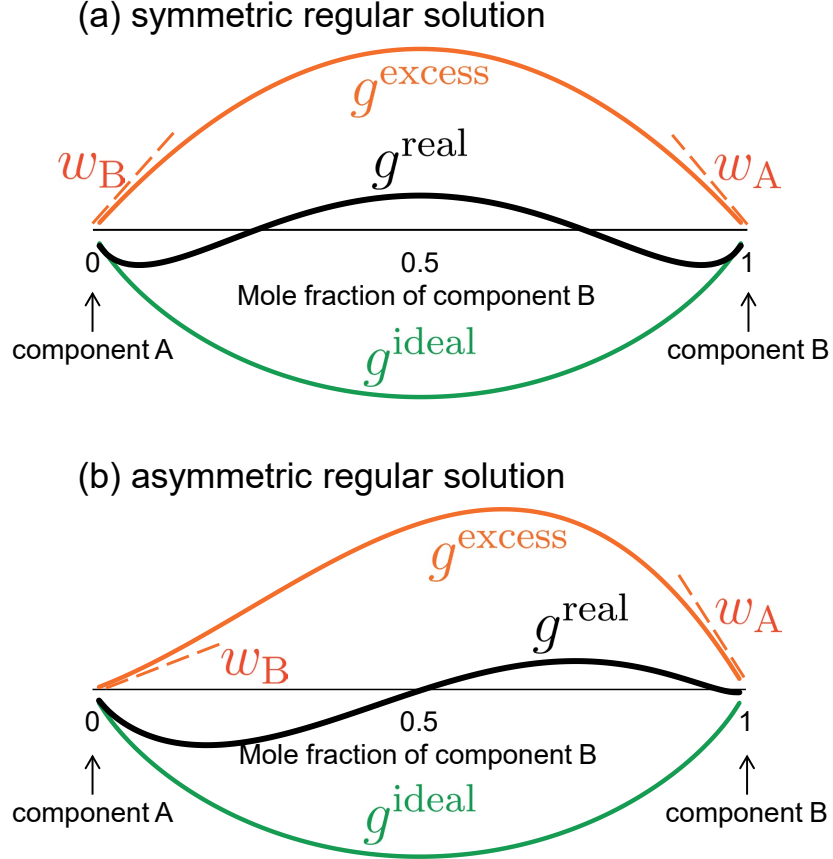


Figure 1: Schematic diagrams of the molar Gibbs energy for regular solutions of two components A and B: (a) symmetric regular solution and (b) asymmetric regular solution. The green curve represents that of an ideal solution g^{ideal} , which is common to both regular solution models. The orange curve represents the molar excess Gibbs energy for a regular solution g^{excess} , and the two models are differentiated based on its shape. The bold black curve represents the sum of these: the molar Gibbs energy of mixing g^{real} . The interaction parameters w_A and w_B are represented by the slopes of the g^{excess} curve at the endpoints on the B side and A side, respectively. In the symmetric model (a), $w_A = w_B$, which is referred to as w_{sym} in the text.

Mathematically, for the symmetric model,

158

$$\left(\frac{\partial g^{\text{real}}}{\partial x}\right)_{T,P} = RT \ln \left(\frac{x}{1-x}\right) + (1-2x)w_{\text{sym}}, \quad (5)$$

$$\left(\frac{\partial^2 g^{\text{real}}}{\partial x^2}\right)_{T,P} = \frac{RT}{x(1-x)} - 2w_{\text{sym}}, \quad (6)$$

and for the asymmetric model,

159

$$\left(\frac{\partial g^{\text{real}}}{\partial x}\right)_{T,P} = RT \ln \left(\frac{x}{1-x}\right) + w_A x(2-3x) + w_B(3x^2-4x+1), \quad (7)$$

$$\left(\frac{\partial^2 g^{\text{real}}}{\partial x^2}\right)_{T,P} = \frac{RT}{x(1-x)} + 2\{w_A(1-3x) + w_B(3x-2)\}, \quad (8)$$

the solutions x when these equations are equal to 0 form the binodal and spinodal curves. Binodal and spinodal curves appear on the cut surfaces of binodal and spinodal surfaces in temperature–pressure–chemical composition space (e.g., Aursand et al., 2017). Hence, either temperature or pressure can be selected for the vertical axis in the lower panel of Fig. 2. This will be explained in section 2.3.

It is well known that silicate melts, which are mixtures of multiple types of oxides, can separate into several distinct phases depending on changes in temperature and pressure, both in natural and industrial compositions: for example, liquid–liquid separation as seen in James (1975); Charlier and Grove (2012). Dehydration of magma is no exception and can be viewed as a separation into liquid phase (water-saturated silicate melt) and vapor phase (silicate-saturated water vapor), i.e., liquid–vapor separation. In this

study, hydrous magma is approximated as a regular solution consisting of two components: anhydrous silicate (melt) and water (vapor), and the thermodynamics of mixing these two components is considered. Therefore, in the following, components A and B are taken to represent silicate and water, respectively. Note that water in magma exists as two molecular species: the molecule $\text{H}_2\text{O}_\text{m}$ and the hydroxyl groups OH (e.g., Stolper, 1982a; 1982b), but we consider them together here. That is, x is the mole fraction of total water. Notably, at and near the silicate end member, a crystalline phase precipitates at low temperatures (e.g., Fig. 4 in Ostrovsky, 1966 for the $\text{SiO}_2\text{--H}_2\text{O}$ system; Fig. 7 in Paillat et al., 1992; and Fig. 3 in Makhluף et al., 2020 for the albite– H_2O system); however, in this study, it is neglected, assuming the amount to be minute and the system to be at a sufficiently high temperature for this assumption to hold, for simplicity.

2.2. Regular solution approximation

2.2.1. Symmetric model vs. asymmetric model

We will consider which model, symmetric or asymmetric, is more appropriate for approximating hydrous magma as a two-component regular solution in the silicate–water system, based on both observational and experimental facts about the behavior of real systems and the mathematical convenience of the models. First, we will discuss the relationship between x_bi and x_spi for each model. In particular, to later utilize knowledge on the silicate-rich side (e.g., the solubility of water in magma), we will focus on the

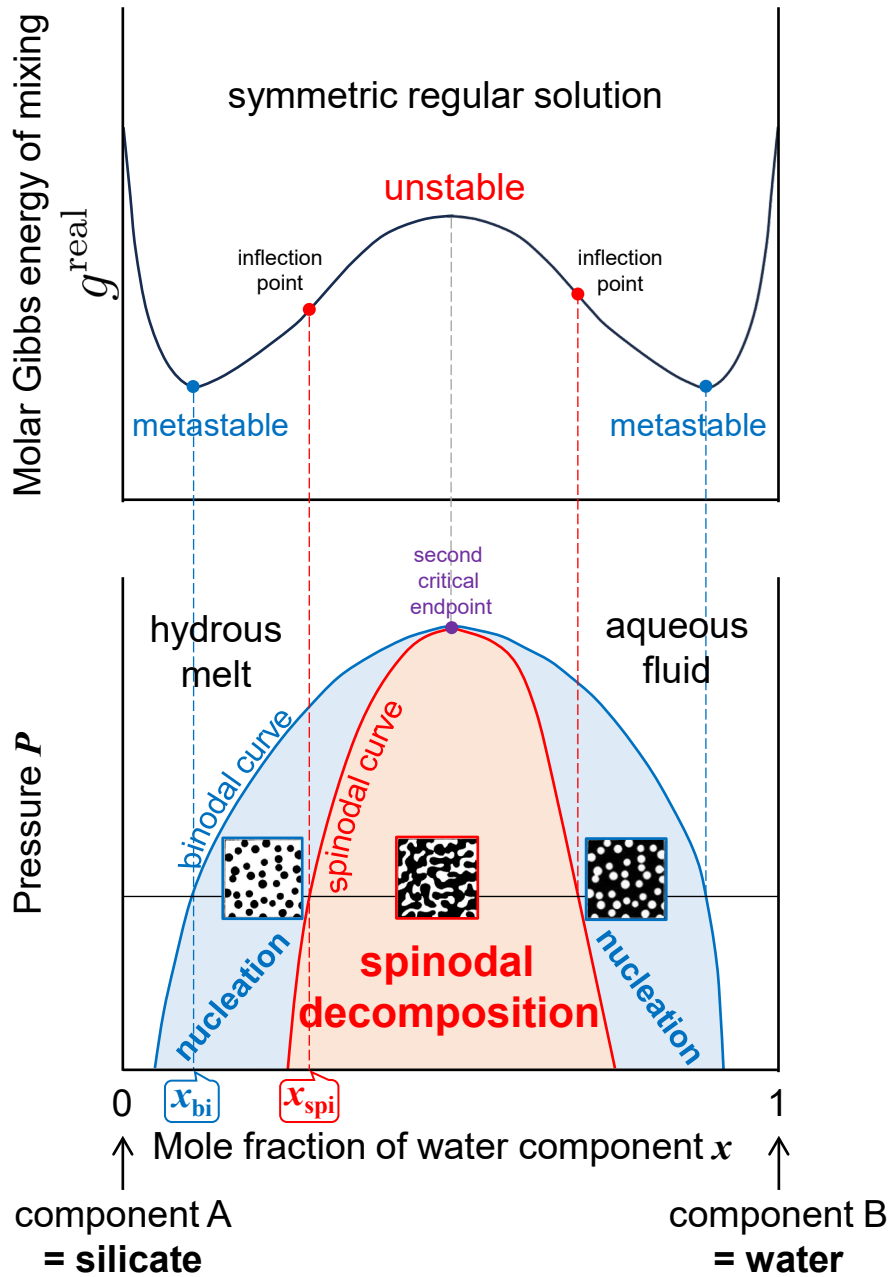


Figure 2: Schematic molar Gibbs energy of mixing g^{real} (upper panel) and corresponding phase diagram (lower panel) for a general two-component symmetric regular solution. In the interval where the g^{real} curve is convex downwards, the system is metastable, and nucleation occurs with clear phase boundaries (surfaces) appearing randomly in space. On the other hand, when the g^{real} curve is convex upward, the system is unstable, and spinodal decomposition occurs, in which the two phases start to separate at a specific wavelength with unclear phase boundaries. 13

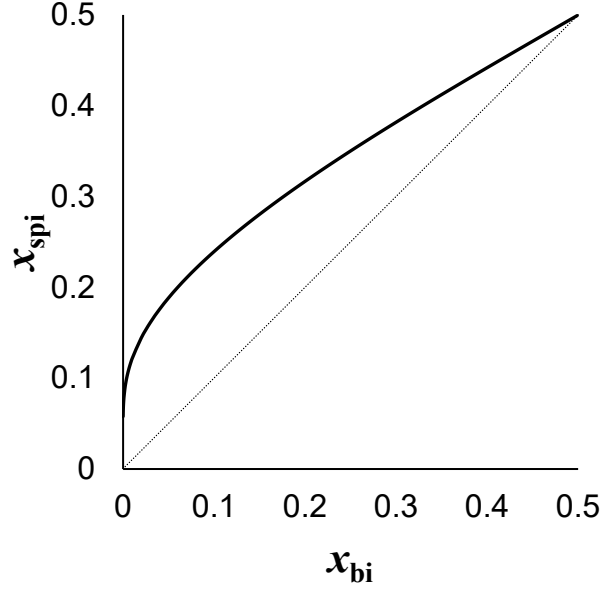


Figure 3: The relation between x_{bi} and x_{spi} at an arbitrary fixed temperature, derived from a series of Eqs. (5) and (6), which represent the first- and second-order derivatives of g^{real} by x . x_{bi} and x_{spi} are the x values that constitute the binodal and spinodal curves, respectively. The range $0 < x < 0.5$ corresponds to the left half of Fig. 1. The relation $x_{\text{spi}} > x_{\text{bi}}$ holds for all the ranges.

range of x smaller than the x at which g^{real} reaches its maximum. 195

For the symmetric model, combining Eqs. (5) and (6) and eliminating 196
 w_{sym} , the following relation between x_{bi} and x_{spi} is derived: 197

$$x_{\text{spi}} = \frac{1}{2} \left\{ 1 - \sqrt{1 - \frac{2(1 - 2x_{\text{bi}})}{\ln \frac{1 - x_{\text{bi}}}{x_{\text{bi}}}}} \right\}. \quad (9)$$

This relation is shown in Fig. 3 in the $0 < x < 0.5$ range, corresponding to 198
the left half area of Fig. 2. 199

On the other hand, in the asymmetric model, the signs of the slopes at 200

both ends of the g^{excess} , i.e., w_A and w_B , are important. When combining
 Eqs. (7) and (8), if both w_A and w_B are positive, the relationship between
 x_{bi} and x_{spi} at a given T or P will be a one-to-one correspondence, just like
 in the symmetric model. As is well-known, the silicate–water system has
 a large miscibility gap (e.g., Kennedy, 1962; Paillat et al., 1992; Shen and
 Keppler, 1997; Bureau and Keppler, 1999), so it is necessary for $g^{\text{excess}} >$
 0 over a wide range of x . Therefore, the assumption that both $w_A > 0$
 and $w_B > 0$ seems reasonable. However, this case may not strictly align
 with the behavior of real systems. For example, at the silicate-rich side,
 when water dissolves, it is slightly exothermic, i.e., $g^{\text{excess}} < 0$, as suggested
 by HF solution calorimetry of hydrous volcanic glasses synthesized at high
 temperature and pressure (Clemens and Navrotsky, 1987; Richet et al., 2004;
 2006). If we trust this experimental result, the correct assumption would be
 that $w_A > 0$ and slightly $w_B < 0$. In other words, the shape of the g^{excess} (and
 thus g^{real}) for hydrous magma is asymmetric, and their peaks should slightly
 shift from $x = 0.5$ (Fig. 4 (a)). But then again, in this case, the relationship
 between x_{bi} and x_{spi} at a given T or P becomes a complex multivalued
 function, as shown in Fig. 4 (b). Specifically, this figure suggests that the
 spinodal curve corresponding to x_{bi} in the range $0 < x_{\text{bi}} < 1/3$ intersects
 with the spinodal curve corresponding to x_{bi} in the range $2/3 < x_{\text{bi}} < 1$,
 which is unrealistic.

Thus, the theoretical equations for a two-component asymmetric regular
 solution do not fit the actual energy curves of g^{excess} (and g^{real}) well.

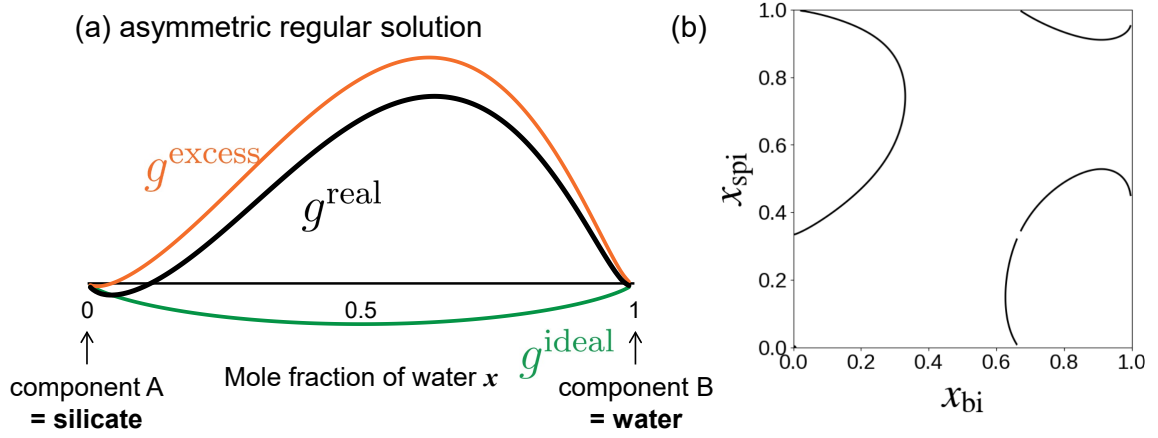


Figure 4: (a) Schematic diagram of the molar Gibbs energy for a realistic hydrous magma, when it was assumed as an asymmetric regular solution of anhydrous silicate (melt) and water (vapor). The meaning of each curve is the same as in Fig. 1. Components A and B correspond to silicate and water, respectively. (b) The relationship between x_{bi} and x_{spi} in a two-component asymmetric regular solution model. An example is shown for the case where $T = 1,000^{\circ}\text{C}$, $w_A = 345.7 \text{ kJ/mol}$, and $w_B = -1.0 \text{ kJ/mol}$.

This issue could be addressed by increasing the number of components 224
to distinguish, thereby increasing the number of unknown interaction 225
parameters w . For example, in the case of a three-component asymmetric 226
regular solution, the expression for g^{excess} can be written as follows (Kakuda 227

$$\begin{aligned}
g^{\text{excess}} = & x_A x_A x_B w_{\text{AAB}} \\
& + x_A x_B x_B w_{\text{ABB}} \\
& + x_B x_B x_C w_{\text{BBC}} \\
& + x_B x_C x_C w_{\text{BCC}} \\
& + x_C x_C x_A w_{\text{CCA}} \\
& + x_C x_A x_A w_{\text{CAA}} \\
& + 2x_A x_B x_C w_{\text{ABC}},
\end{aligned} \tag{10}$$

where w_{ijk} is the interaction parameter between particles in a triplet
 consisting of three particles. Nishiwaki (2023) distinguished between the
 molecular species of water (molecular water H_2O_m and hydroxyl groups OH)
 and considered hydrous magma as a three-component system consisting of
 bridging oxygen of anhydrous silicate and these water species. Additionally,
 he attempted to determine the values of the seven w_{ijk} parameters and
 the shapes of g^{excess} (and g^{real}) over a wide range of temperatures and
 pressures. However, this problem is highly challenging from a linear algebraic
 standpoint, and the values reported in Nishiwaki (2023) are likely to be
 incorrect. We are currently working toward resolving this issue (Nishiwaki
 and Fukuya, in prep.). In the end, although we know that the shape of g^{excess}
 (and g^{real}) is complex, as shown in Fig. 4 (a), for now, we have no choice

but to compromise and approximate hydrous magma as a two-component
symmetric regular solution consisting of silicate and water. As a result,
this approach is consistent with the scheme adopted by Allabar and Nowak
(2018).

2.2.2. Consistency with known phase diagrams

Next, we will evaluate the validity of the two-component symmetric
regular solution approximation by comparing it with the already-known
phase diagrams. In Fig. 2, the regions on the silicate-rich and water-rich
sides at pressures higher than the binodal curve, correspond to hydrous melt
and aqueous fluid, respectively. Thus, when a pressure change occurs that
cuts the binodal curve at a fixed chemical composition, the reaction “magma
(supercritical fluid) \leftrightarrow water-saturated silicate melt (hydrous melt) + almost
pure water vapor (aqueous fluid)” occurs. The rightward reaction indicates
exsolution with decompression, whereas the leftward reaction indicates
mutual dissolution with compression. For example, according to the results of
high-temperature and high-pressure experiments shown in Fig. 3 of Makhlu
et al. (2020), for the albite–water system at 900°C, the second critical
endpoint (the vertex of the miscibility gap) is in the range of 1.25–1.40 GPa
and 42–45 wt%, i.e., $x = 0.57$ – 0.60 (on a single oxygen basis). While some
experimental studies have indicated that the position of the second critical
endpoint may vary depending on the temperature and chemical composition
of the silicate (Bureau and Keppler, 1999; Sowerby and Keppler, 2002), in

this study, I assume that it does not deviate significantly from $x = 0.5$ to use the symmetric regular solution approximation, as mentioned in the previous section. This assumption may be somewhat forceful, but it is the simplest model we can present at this stage, and it will serve as a baseline for comparison when the detailed shape of the Gibbs energy is determined in the future, and the model is updated.

2.3. Spinodal decomposition with pressure change

Since spinodal decomposition is a phenomenon discovered in the field of inorganic materials such as ceramics and alloys (e.g., Cahn, 1965), it is typically discussed in terms of phase separation into solid–solid/solid–liquid/liquid–liquid systems that occur with decreasing temperature at normal pressure. Thus, temperature is typically used as the vertical axis when drawing phase diagrams. In contrast, when considering whether spinodal decomposition occurs in the phase separation of magma into gas–liquid systems, I assumed constant temperature and focused on the phase separation that occurs during decompression, since water solubility is much more dependent on pressure than temperature. Therefore, I adopted pressure as the vertical axis in the phase diagram in Fig. 2. It has been suggested that, in nature, magma degassing may be more efficiently achieved through heating caused by the latent heat of crystallization, viscosity, and friction rather than decompression (e.g., Lavalée et al., 2015). However, typically, decompression experiments are conducted at a constant

temperature, and so far, scenarios of spinodal decomposition have been
 proposed based solely on the results of such experiments (Gonnermann and
 Gardner, 2013; Allabar and Nowak, 2018; Allabar et al., 2020b; Sahagian
 and Carley, 2020; Gardner et al., 2023; Marks and Nowak, 2024; Hummel et
 al., 2024). Therefore, focusing on the pressure direction to test the validity
 of this scenario is not necessarily a flawed assumption.

3. Calculation methods

3.1. Relation between water solubility curve and binodal curve, and calculation of the spinodal curve

The section for $x < 0.5$ of the binodal curve on the x - P plane at constant
 T , shown in the lower panel of Fig. 2, should coincide with the solubility
 curve of water in the silicate melt at that temperature with respect to pressure
 change. In other words, the water solubility $c(P)$ in the silicate melt is equal
 to $x_{\text{bi}}(P)$, which constitutes the binodal curve. From this and the relation Eq.
 (9) between x_{bi} and x_{spi} , we can calculate the value of x_{spi} that constitutes
 the spinodal curve. The value of the silicate–water interaction parameter
 $w_{\text{sym}}(P)$ at a fixed temperature can also be determined by substituting the
 value of $x_{\text{bi}}(P)$ into Eq. (5) or the value of $x_{\text{spi}}(P)$ into Eq. (6).

3.2. Conditions on the temperature, chemical composition, and water solubility in magma

Three types of silicate melts are assumed for temperature and chemical
 composition: K-phonolitic melt at 1,050°C, basaltic melt at 1,100°C, and

albite melt at 900°C. For the phonolitic melt, the conditions are the
 same as those used in all experiments of Allabar and Nowak (2018).
 Basaltic and albite melts were chosen to compare and examine the spinodal
 curves' behavior at higher pressures. The temperatures employed are those
 at which the pressure dependence of water solubility in the melt was
 already systematically determined from high-temperature and high-pressure
 experiments. According to Iacono-Marziano et al. (2007), who performed
 decompression experiments using AD79 Vesuvius pumice as did Allabar and
 Nowak (2018), since the water solubility in K-rich phonolitic melt at 1,050°C
 agrees well with the value calculated from the empirical model of Moore et
 al. (1998), their formula was also used in this study in the range 0.1–300
 MPa. Note that Moore et al. (1998) defined the mole fraction of water by
 treating each oxide (e.g., SiO₂ and Al₂O₃) as one unit, but this definition is
 no longer in common use, and here, the mole fraction was converted to the
 currently commonly used single-oxygen basis values (see Section 1.2 in Zhang,
 1999). The water solubility in the basaltic melt at 1,100°C was obtained by
 digitizing the fitting curve of the experimentally determined values for \lesssim 600
 MPa, as shown in Fig. 2 of Hamilton et al. (1964). The water solubility in
 the albite melt at 900°C was also obtained by digitizing the fitting curve of
 the experimentally determined values for \lesssim 1000 MPa, as shown in Fig. 8 of
 Burnham and Jahns (1962).

4. Calculation results

328

The binodal and spinodal curves drawn on the x - P plane for the three
silicate–water systems are shown in Fig. 5. The geometric characteristics
of both curves are similar, regardless of the silicate composition. Fig. 6 in
Allabar and Nowak (2018) and Fig. 1 in Sahagian and Carley (2020) show a
conceptual phase diagram in which both the binodal and spinodal curves are
convex upward over the entire chemical composition range, with a large area
inside the spinodal curve. The lower panel of Fig. 2 in this study is identical.
However, when considering their actual position and shape quantitatively
based on chemical thermodynamics, the solubility curve (= binodal curve)
is convex downward at $\lesssim 400$ MPa (approximately the relation $c(P) \propto P^{0.5}$
holds); therefore, the spinodal curve is also convex downward. In the pressure
range examined in this study, the spinodal curve is situated at a much lower
pressure relative to the binodal curve when fixed at a certain water content.
For example, at $x = 0.10$, the water solubility (wt%), P_{bi} (MPa), and P_{spi}
(MPa) for the phonolitic melt, basaltic melt, and albite melt are (5.4, 219,
 < 1), (5.2, 239, 6), and (5.8, 166, 10), respectively. Furthermore, as x
increases, the corresponding P_{spi} gradually transitions to the high-pressure
side, but the difference from P_{bi} is still very large. In other words, the
nucleation region is much broader than the spinodal decomposition region,
at least in the $x < 0.25$ range plotted in Fig. 5. For example, in the case of
albite melt, $P_{\text{bi}} = 1000$ MPa, which corresponds to approximately $P_{\text{spi}} = 190$
MPa.

350

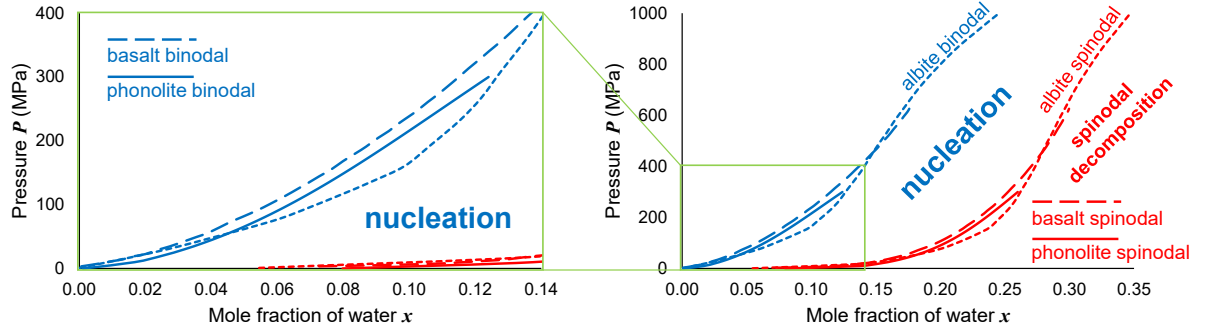


Figure 5: Binodal (blue) and spinodal (red) curves for hydrous 1,050°C K-phonolitic (solid line), 1,100°C basaltic (dashed line), and 900°C albite (dotted line) melts in the pressure range 0.1–1000 MPa. The left panel shows an enlargement of the right panel at pressures below 400 MPa. The binodal curves correspond to the water solubility curves in the melt for each chemical composition (Moore et al., 1998; Hamilton et al., 1964; Burnham and Jahns, 1962). The position of spinodal curves was determined from the position of binodal curves and Eq. (9).

The calculation results for $w(P)$ are shown in Fig. 6. Although w is large 351
at 0.1 MPa (phonolite: 75 kJ/mol, basalt: 85 kJ/mol, and albite: 95 kJ/mol), 352
for all three chemical compositions it monotonically decreases rapidly with 353
increasing pressure over the entire pressure range. This behavior is consistent 354
with the fact that the mutual dissolution of silicate and water proceeds at 355
higher pressures at a fixed temperature, which narrows the miscibility gap. 356

5. Discussion 357

5.1. Can spinodal decomposition occur during decompression-induced 358 vesiculation of magma? 359

First, I focus on the pressure range approximately below 300 MPa, where 360
almost all decompression experiments have been conducted. All nucleation 361
pressure values in 88 previous experiments, from Gardner et al. (1999) to 362

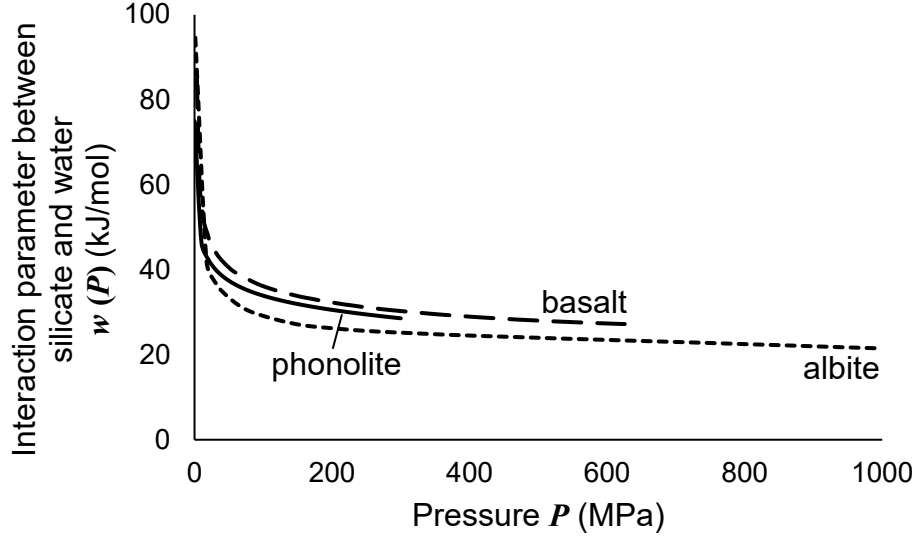


Figure 6: Calculation results of the interaction parameter between silicate and water $w(P)$ for hydrous K-phonolitic melt at 1,050°C and 0.1–300 MPa (solid line), basaltic melt at 1,100°C and 0.1–625 MPa (dashed line), and albite melt at 900°C and 0.1–1000 MPa (dotted line).

Le Gall and Pichavant (2016), compiled and calculated by Shea (2017), fall within the nucleation region shown in Fig. 5 if variations in melt chemical composition are not considered. Additionally, all Allabar and Nowak (2018) experimental runs were performed in the range of the initial pressure of 200 MPa to final pressures of 70–110 MPa. Since the final pressures are higher than P_{spi} , the nucleation pressure of these runs inevitably falls into the nucleation region. Therefore, the innovative scenario proposed by Allabar and Nowak (2018) and Sahagian and Carley (2020)—spinodal decomposition during decompression-induced vesiculation of magma—cannot occur in the pressure range of magmatic processes in the continental crust at depths of several hundred MPa. In addition, since $P_{\text{spi}} \ll P_{\text{bi}}$ as shown in Fig. 5,

for spinodal decomposition to occur without nucleation, it is necessary to
maintain sufficient supersaturation, despite a very large decompression from
an initial pressure higher than P_{bi} to a pressure lower than P_{spi} . Gardner
et al. (2023) stated that we must consider the overlap of various bubble
formation mechanisms, including spinodal decomposition, to interpret BND
and bubble size distributions in natural pyroclasts, I argue that we can focus
only on homogeneous and heterogeneous nucleation as previously envisaged.
Note that to confirm indeed that spinodal decomposition is unlikely to
occur, it would likely be necessary to conduct runs with relatively rapid
decompression to pressures lower than P_{spi} . However, rapid decompression
to near atmospheric pressure increases the possibility of capsule rupture,
and bubbles' rapid expansion and coalescence may drastically overwrite
the geometric arrangement of vesicular textures from its original state.
Additionally, as mentioned in 2.3, in some natural systems where degassing is
primarily driven by heating rather than decompression, the effective amount
of decompression may become larger, making it possible that spinodal
decomposition cannot be completely ruled out.

On the other hand, in regions of higher pressure and higher water
content outside the drawn area of Fig. 5, P_{spi} asymptotically approaches
 P_{bi} , and spinodal decomposition is more likely to occur. In other words,
spinodal decomposition may occur if decompression passes near the top of the
second critical endpoint. In addition, because the second critical endpoint
of silicate–water systems has been reported to shift to lower temperatures

and pressures with increasing amounts of alkali metal oxides (e.g., Na_2O 397
 and K_2O) in the silicate (Bureau and Keppler, 1999; Sowerby and Keppler, 398
 2002), Allabar and Nowak (2018) suggested that spinodal decomposition 399
 at low pressures may be more likely to occur in alkali-rich phonolite melts 400
 than in other silicic silicates. However, as long as the symmetric regular 401
 solution approximation is assumed, the shift of the second critical endpoint 402
 to lower pressures, i.e., the shift of the binodal curve to lower pressures, is 403
 accompanied by a shift of the spinodal curve to lower pressures because 404
 x_{bi} and x_{spi} change in tandem, as shown in Fig. 3. In this case, the 405
 region of spinodal decomposition shown in Fig. 5 would be narrower, 406
 and spinodal decomposition would be less likely to occur. Therefore, if 407
 spinodal decomposition occurs in the phonolitic melt, the binodal curve 408
 of the phonolite–water system is expected to have a highly asymmetric 409
 shape to which the symmetric regular solution approximation cannot be 410
 applied. This might be related to the effective ionic radius of potassium 411
 (1.38 Å) that is abundant in the phonolitic melt and is as large as that of 412
 oxygen (1.40 Å) (Shannon, 1976). The packing ratio is higher than that in 413
 alkali-poor silicates (e.g., albite and rhyolite). Still, the shape of the binodal 414
 curve of the phonolite–water system has yet to be determined and requires 415
 exploration in detail using high-temperature and high-pressure experiments 416
 in the future. Considering additional complexities not accounted for in the 417
 symmetric model used in this study, it is difficult to rule out the possibility 418
 of spinodal decomposition completely. 419

5.2. Consideration of kinetic effects

The discussions in the previous sections were based on equilibrium thermodynamics; thus, static binodal and spinodal curves were determined. However, in reality, during phase separation associated with pressure changes, kinetic effects arise due to the differences in the dynamic properties of silicate and water. As a consequence, the positions of the dynamic binodal and spinodal curves do not coincide with those of the static ones.

Wang et al. (2021) conducted an in-situ observation of the phase separation process of peralkaline aluminosilicate ($\text{Na}_3\text{AlSi}_5\text{O}_{13}$)–water system in a single-phase supercritical fluid near the second critical endpoint (approximately 700°C and 1 GPa) using a hydrothermal diamond anvil cell. As a result, they observed that, at specific composition ratios (37–51 wt% aluminosilicate), the network of hydrous silicate melt emerged as the temperature decreased, and two phases separated, with aqueous fluid enclosed within the silicate melt (spinodal decomposition). Additionally, Raman spectroscopy data collected in situ revealed that polymerized aluminosilicate species were selectively incorporated into the silicate melt, while silica monomers were selectively incorporated into the aqueous fluid. They interpreted this phenomenon by referring to the viscoelastic phase separation (VPS) theory for polymer solutions (Tanaka, 1994), suggesting that the relatively large molecules of the silicate polymer and the small molecules of water have significantly different relaxation timescales, i.e., viscoelastic properties, and thus, they undergo phase separation in a

network-like structure.

Their experimental results using a peralkaline composition could offer a new perspective in interpreting the experimental results of Allabar and Nowak (2018), which also employed alkali-rich phonolite. Contrary to the traditional image of spinodal decomposition (the so-called “intertwined structure” shown in Fig. 2), the experimental observation that phase separation occurs in a network-like structure suggests that the inference made from the experimental observations in Allabar and Nowak (2018)—where the spatial distribution of bubbles appeared to follow a specific wavelength and was attributed to spinodal decomposition—may not hold.

According to Wang et al. (2021), at constant pressure, the dynamic spinodal curve shifts to lower temperatures compared to the static one, as shown in (1) of Fig. 7, where the spinodal curve was drawn with the negative slope, assuming that it would be similar to the negative slope of the phase boundary (binodal curve) appearing in the T – P plane at a fixed composition. In this case, at a fixed temperature, the spinodal curve shifts to the lower pressure side: (2) in Fig. 7. In other words, if the kinetic effects observed in their experiments were to appear in an isothermal decompression system, they would likely occur at pressures lower than the static spinodal pressure P_{spi} determined from thermodynamic calculations. However, as discussed in the previous section, within the pressure–composition (water content) range where decompression experiments have been conducted, P_{spi} is very low and lower than all the final pressures. Therefore, the scenario proposed by Allabar

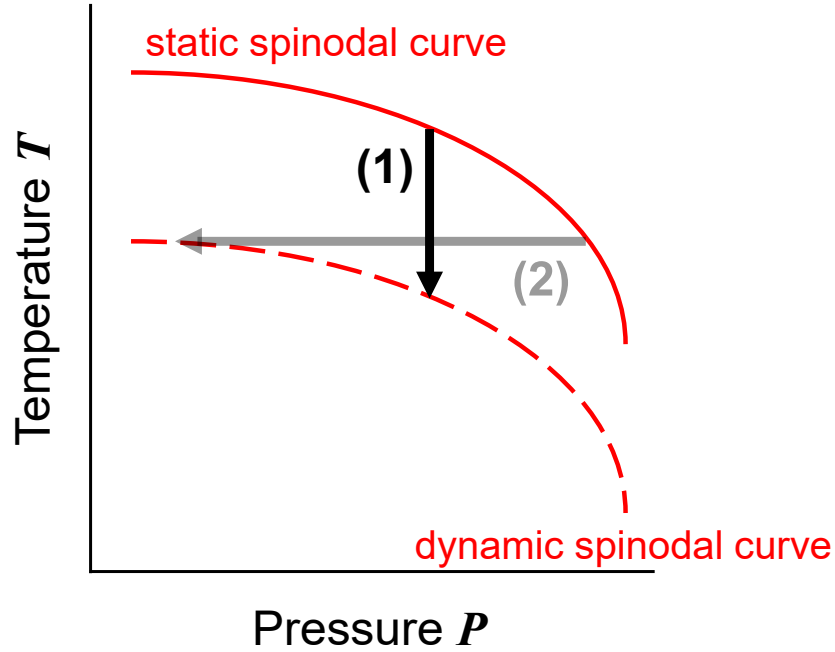


Figure 7: The schematic relationship between the static and dynamic spinodal curves on the T – P plane for a fixed composition. (1) At constant pressure, the dynamic spinodal curve shifts to the lower temperature side compared to the static one (Wang et al., 2021). (2) In this case, at a fixed temperature, the spinodal curve shifts to the lower pressure side.

and Nowak (2018) would be even less likely to occur.

5.3. On the compilation of decompression-experimental results

Allabar and Nowak (2018) plotted their newly obtained experimental data and selected data from previous decompression experiments (Iacono-Marziano et al., 2007; Marxer et al., 2015; Preuss et al., 2016) conducted under the same chemical composition and physical conditions (phonolitic melt, 1,050°C, initial pressure 200 MPa, and continuous decompression) on the decompression rate–BND plane (see Fig. 8 in their

paper). The BND values of those data were all in the same order of
 magnitude, almost independent of the decompression rate. In other words,
 these data are non-harmonic with the classical nucleation theory’s numerical
 prediction: $\text{BND} \propto |\text{decompression rate}|^{1.5}$ (BND decompression rate meter
 from Toramaru, 2006). The authors considered that spinodal decomposition,
 rather than nucleation, might be occurring to explain these experimental
 results.

The selection criteria for past data were not described in Allabar and
 Nowak (2018) but were detailed in Allabar et al. (2020a, b). In those studies,
 vesicle shrinkage during cooling and the initial water content dependence
 of BND in hydrous phonolitic melt were thoroughly investigated through
 precisely repeated experiments. They revealed that the several factors,
 denoted in [Appendix B](#), are essential in decompression experiments to
 determine BND. Only the data obtained under these protocols (hereafter
 referred to as the “good protocols”) are considered worth discussing in terms
 of consistency with the BND decompression meter (Allabar et al., 2020b).
 Though the good protocols were established through a series of experiments
 using phonolitic melt, since each is based on rational reasoning, they should
 be applied when conducting experiments with other compositions in the
 future.

I replotted all the experimental data on phonolitic melt at 1,050°C,
 initial pressure 200 MPa, and continuous decompression in Fig. 8. Here,
 in addition to the four papers mentioned earlier, data from Allabar et al.

(2020b) Table 2 are referenced. The data that meet the good protocols
are represented by plots with thick borders. As discussed in Allabar et
al. (2020b), since BND has an initial water content dependence, there is
some vertical variation even within populations of high BND values, but the
variation is smaller compared to the data that mostly do not meet the good
protocols from Iacono-Marziano et al. (2007) and Marxer et al. (2015). Even
though Marxer et al. (2015)’s data does not satisfy the good protocols, it
is harmonic with the BND decompression rate meter. Additionally, several
previous papers reported harmonic results with the BND decompression rate
meter (e.g., Mourtada-Bonnefoi and Laporte, 2004; Hamada et al., 2010),
but they also seem not to satisfy the good protocols. In summary, there
is a peculiar inconsistency where some data that do not satisfy the good
protocols are in harmony with the BND decompression rate meter, while
data that do satisfy the good protocols are not. I suspect that there are
two main possible causes for this inconsistency. The first possibility, as
mentioned in 5.1, is the uniqueness of the composition of phonolitic melt. It
would be worth investigating how the BND decompression rate dependency
behaves in the rhyolitic melt, which has relatively low alkali content and
a wealth of past experimental examples when conducted following the good
protocols. The second possibility, already discussed by Allabar et al. (2020b),
is that the potential for heterogeneous nucleation on the surfaces of nanolites
or ultrananolites such as Fe–Ti oxides (e.g., Mujin and Nakamura, 2014)
cannot be excluded entirely. If the number density of such oxide crystals is

a significant control factor for BND, then the BND obtained in experiments
may not necessarily follow the BND decompression rate meter.

It might also be worth considering how to explain the independence
of BND on the decompression rate without using spinodal
decomposition—specifically, developing a new CNT-based theory, which
could encompass this phenomenon, by improving the BND decompression
rate meter. Assuming that all the experimental results plotted in Fig. 8
are equally reliable, they suggest that the decompression rate dependence
of BND in phonolitic melts is extremely varied. It is known from magma
crystallization experiments that the crystal number density can depend on
the cooling rate (proportional to the $3/2$ power of the cooling rate; consistent
with the CNT-based prediction assuming diffusion-limited growth) as in
Toramaru (2001) or shows no dependence, or even decreases (Martel and
Schmidt, 2003; Cichy et al., 2011; Andrews and Befus, 2020). Toramaru and
Kichise (2023) proposed that this wide range of cooling rate dependence can
be explained by varying the pre-exponential factor of the nucleation rate
and the surface tension. If there were a bubble version of this crystallization
model, it might be possible to explain the wide variety of decompression
rate dependence of BND (Toramaru, 2025).

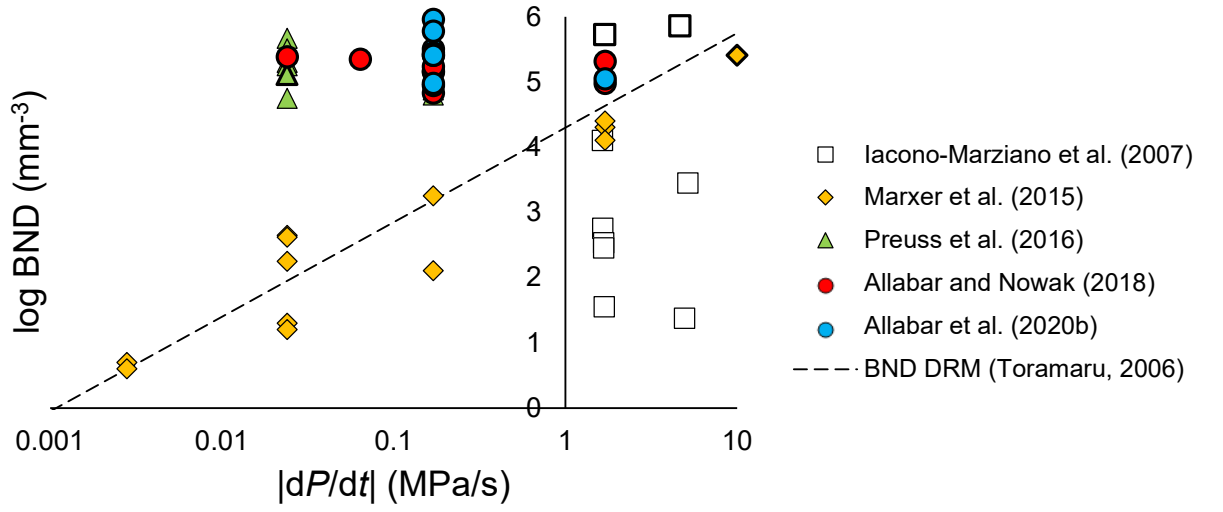


Figure 8: Results of decompression experiments using hydrous K-phonolitic melt from previous works (Iacono-Marziano et al., 2007; Marxer et al., 2015; Preuss et al., 2016; Allabar and Nowak, 2018; Allabar et al., 2020b). The dotted line is the theoretical prediction calculated by BND decompression rate meter, bubble number density decompression rate meter, from Toramaru (2006). The plots with thick borders represent reliable experimental data that meet the “good protocols” for decompression experiments (refer to the main text) described in Allabar et al. (2020b).

5.4. *Application: Estimation of the surface tension between the melt and* 539
bubble nucleus 540

When quantitatively considering the time evolution of the initial stage 541
of magma vesiculation, values for several physical parameters (e.g., diffusion 542
coefficient of water in the melt, viscosity of the melt, and surface tension 543
between the melt and bubble nucleus) are required, as in the case of the BND 544
decompression rate meter by Toramaru (2006). Many of these parameters 545
have been carefully determined through past experiments. Still, even though 546
the “microscopic” surface tension between the melt and (homogeneous 547
spherical) bubble nucleus, σ , is a powerful parameter governing nucleation, its 548
direct measurement is currently impossible. Therefore, it has been calculated 549
only by fitting the integral value of the CNT-based nucleation rate J over 550
time with the obtained BND from decompression experiments: the inversion 551
of BND using the CNT formula (e.g., Mourtada-Bonnefoi and Laporte, 2004; 552
Cluzel et al., 2008; Hamada et al., 2010). However, since the detailed time 553
evolution of J is unknown, σ has not been determined with high precision, 554
and considerable uncertainty exists (Shea, 2017). See [Appendix A](#) for 555
the detailed expression of the equation of J in CNT (e.g., Hirth et al., 556
1970). It has been found that σ obtained via the CNT formula tends to 557
be significantly smaller than the “macroscopic” surface tension σ_∞ at the 558
flat interface between the melt and vapor, directly measured by Bagdassarov 559
et al. (2000) (e.g., Hamada et al., 2010). 560

The reason why $\sigma < \sigma_\infty$ occurs was interpreted by Gonnermann and 561

Gardner (2013) as follows. According to the recent non-classical nucleation theory, the interface between the original and new phases loses sharpness and diffuses under non-equilibrium conditions (e.g., Chapter 4 in Kelton and Greer, 2010). Such interfacial diffusion should also occur during the vesiculation of magma with supersaturated water, which is no longer soluble due to decompression. In other words, the relationship $\sigma = \sigma_\infty$ (capillary approximation) holds at the binodal pressure P_{bi} , but as the supersaturation increases, σ is expected to decrease, and when the spinodal pressure P_{spi} is reached, where a distinct interface is expected to vanish, σ should become zero. They formulated this idea and derived σ using a completely different approach from the BND inversion through CNT. However, at that time, P_{spi} was unknown, so it was considered a hypothetical parameter, and the uncertainty was incorporated into the mathematical treatment. In this study, although a highly simplified equilibrium thermodynamic model is used, P_{spi} was determined for the first time. By substituting this into the equation for the dependence of σ on the degree of supersaturation, the estimation of σ is expected to be improved to a more straightforward way (Nishiwaki, in prep.).

6. Conclusions

I calculated the positions of the binodal and spinodal curves on the chemical composition–pressure plane by assuming that hydrous magma is a two-component symmetric regular solution of silicate and water and using the

chemical thermodynamic equation and experimental data on water solubility
in magma. The spinodal curve located significantly lower-pressure side than
the binodal curve at pressures sufficiently below the second critical endpoint.
The pressure ranges of all previous decompression experiments fell between
these two curves. Therefore, decompression-induced vesiculation of magma
occurs through nucleation, and spinodal decomposition is highly unlikely,
in the magmatic processes associated with volcanic eruptions in most
natural continental crusts. This result contradicts the recent inference that
spinodal decomposition can occur based on observations of the bubble texture
of decompression-experimental products. Additionally, by combining the
spinodal pressure determined in this study with the non-classical nucleation
theory, it may be possible to easily estimate the surface tension between the
silicate melt and bubble nucleus, which has not been accurately determined.

Appendix A. Equation of the nucleation rate in classical nucleation theory (CNT)

The equation for J in CNT (Hirth et al., 1970) is as follows:

$$J = \frac{2n_0^2 D_{\text{H}_2\text{O}} \bar{V}_{\text{H}_2\text{O}}}{a_0} \sqrt{\frac{\sigma}{k_{\text{B}} T}} \exp \left\{ -\frac{16\pi\sigma^3}{3k_{\text{B}} T} (P_{\text{B}}^* - P_{\text{M}}) \right\}, \quad (\text{A.1})$$

where n_0 is the number of water molecules per unit volume, $D_{\text{H}_2\text{O}}$ is the
diffusivity of total water in the melt, $\bar{V}_{\text{H}_2\text{O}}$ is the partial molar volume of
water in the melt, a_0 is the average distance between water molecules in

the melt, σ is the “microscopic” surface tension between the melt and the
bubble nucleus, k_B is the Boltzmann’s constant, T is the temperature, P_B^* is
the internal pressure of the critical bubble nucleus, and P_M is the pressure of
the melt.

Appendix B. “Good protocols” established through a series of decompression experiments using phonolitic melt

Based on the results of a series of decompression experiments conducted
using phonolitic melt (Iacono-Marziano et al., 2017; Marxer et al., 2015;
Preuss et al., 2016; Allabar and Nowak, 2018; Allabar et al., 2020b), Allabar
et al. (2020b) proposed that ideal experimental products can be obtained
by following the protocols outlined below: (a) Homogeneous, bubble-free
glass cylinders should be used as starting materials, encapsulated in noble
metal tubes containing water for hydration at slightly H_2O undersaturated
superliquidus conditions. This setup prevents the presence of fluid bubbles
before decompression. (b) The sample should be continuously decompressed
at a reasonable decompression time scale to mitigate the drainage of dissolved
 H_2O from the melt volume into heterogeneously formed vesicles at the capsule
wall. This approach helps to prevent the potential detachment and movement
of heterogeneously nucleated vesicles from the capsule walls into the melt
volume. (c) To determine the initial BND, the decompression should be
terminated at a reasonable final pressure to avoid bubble coalescence which
would reduce the initial BND. (d) To determine bubble growth and the onset

of bubble coalescence and to observe a possible second bubble formation 625
event, a comprehensive set of experiments with small steps in final pressure 626
down to low pressure is necessary. (e) Subsequent quench of the partially 627
degassed sample should be as fast as possible to minimize vesicle shrinkage. 628
A cooling rate of $\sim 44^\circ\text{C/s}$ limits bubble shrinkage, inhibits quench crystal 629
formation and avoids the formation of tension cracks. 630

Acknowledgments

The author would like to thank Marcus Nowak for sharing numerous detailed and insightful comments on the experiments and results from their team, which significantly contributed to the improvement of the manuscript. The author is grateful to Yosuke Yoshimura for discussing spinodal decomposition in gas–liquid systems induced by pressure changes. The author also appreciates Atsushi Toramaru for his insightful comments on the similarity to the latest crystallization models, which contributed to enhancing the content of this paper. Special thanks go to Takeshi Ikeda for many discussions on the fundamentals of the thermodynamics of silicate–water immiscibility. The reading circle for a glass science text with Shigeru Yamamoto inspired the author for this study. Shumpei Yoshimura provided the author with some methods for calculating the mole fraction of water in magma. The content of this paper was deepened after the discussion with Hidemi Ishibashi and Takayuki Nakatani. The manuscript has been significantly improved through MP and Mathieu Colombier’s peer review, as

well as the generous handling by Editor Chiara Maria Petrone. This work was supported by JSPS KAKENHI Grant Number JP23K19069. The author would like to thank Editage (www.editage.jp) for English language editing.

References

Allabar, A., and Nowak, M., 2018. Message in a bottle: Spontaneous phase separation of hydrous Vesuvius melt even at low decompression rates. *Earth Planet. Sci. Lett.* **501**, 192–201. <https://doi.org/10.1016/j.epsl.2018.08.047>

Allabar, A., Dobson, K. J., Bauer, C. C., and Nowak, M., 2020a. Vesicle shrinkage in hydrous phonolitic melt during cooling. *Contrib. Mineral. Petrol.* **175** (3), 21. <https://doi.org/10.1007/s00410-020-1658-3>

Allabar, A., Salis Gross E., and Nowak, M., 2020b. The effect of initial H₂O concentration on decompression-induced phase separation and degassing of hydrous phonolitic melt. *Contrib. Mineral. Petrol.* **175** (3), 22. <https://doi.org/10.1007/s00410-020-1659-2>

Andrews, B. J., and Befus, K. S., 2020. Supersaturation nucleation and growth of plagioclase: a numerical model of decompression-induced crystallization. *Contrib. Mineral. Petrol.* **175** (3), 23. <https://doi.org/10.1007/s00410-020-1660-9>

Aursand, P., Gjennestad, M. A., Aursand, E., Hammer, M., and Wilhelmsen, Ø., 2017. The spinodal of single- and multi-component fluids and its role in the development of modern equations of state. *Fluid Phase*

Equilib. **436**, 98–112. <https://doi.org/10.1016/j.fluid.2016.12.018>

Bagdassarov, N., Dorfman, A., and Dingwell, D. B., 2000. Effect of alkalis, phosphorus, and water on the surface tension of haplogranite melt. *Am. Mineral.* **85** (1), 33–40. <https://doi.org/10.2138/am-2000-0105>

Bureau, H., and Keppler, H., 1999. Complete miscibility between silicate melts and hydrous fluids in the upper mantle: experimental evidence and geochemical implications. *Earth Planet. Sci. Lett.* **165** (2), 187–196. [https://doi.org/10.1016/S0012-821X\(98\)00266-0](https://doi.org/10.1016/S0012-821X(98)00266-0)

Burnham, C. W., and Jahns, R. H., 1962. A method for determining the solubility of water in silicate melts. *Am. J. Sci.* **260** (10), 721–745. <https://doi.org/10.2475/ajs.260.10.721>

Cahn, J. W., 1965. Phase separation by spinodal decomposition in isotropic systems. *J. Chem. Phys.* **42** (1), 93–99. <https://doi.org/10.1063/1.1695731>

Cahn, J. W., and Hilliard, J. E., 1959. Free energy of a nonuniform system. III. Nucleation in a two-component incompressible fluid. *J. Chem. Phys.* **31** (3), 688–699. <https://doi.org/10.1063/1.1730447>

Cassidy, M., Manga, M., Cashman, K., and Bachmann, O., 2018. Controls on explosive-effusive volcanic eruption styles. *Nat. Commun.* **9** (1), 1–16. <https://doi.org/10.1038/s41467-018-05293-3>

Charlier, B., and Grove, T. L., 2012. Experiments on liquid immiscibility along tholeiitic liquid lines of descent. *Contrib. Mineral. Petrol.* **164**, 27–44. <https://doi.org/10.1007/s00410-012-0723-y>

Cichy, S. B., Botcharnikov, R. E., Holtz, F., and Behrens, H., 2011. Vesiculation and microlite crystallization induced by decompression: a case study of the 1991–1995 Mt Unzen eruption (Japan). *J. Petrol.* **52** (7–8), 1469–1492. <https://doi.org/10.1093/petrology/egq072>

Clemens, J. D., and Navrotsky, A., 1987. Mixing properties of $\text{NaAlSi}_3\text{O}_8$ melt– H_2O : new calorimetric data and some geological implications. *J. Geol.* **95** (2), 173–188. <https://doi.org/10.1086/629118>

Cluzel, N., Laporte, D., Provost, A., and Kannevischer, I., 2008. Kinetics of heterogeneous bubble nucleation in rhyolitic melts: implications for the number density of bubbles in volcanic conduits and for pumice textures. *Contrib. Mineral. Petrol.* **156** (6), 745–763. <https://doi.org/10.1007/s00410-008-0313-1>

Debenedetti, P. G., 2000. Phase separation by nucleation and by spinodal decomposition: Fundamentals. In: Kiran, E., Debenedetti, P. G., Peters, C. J. (Eds.), *Supercritical Fluids*. Nato Science Series **366**, 123–166. https://doi.org/10.1007/978-94-011-3929-8_5

Gardner, J. E., Hilton, M., and Carroll, M. R., 1999. Experimental constraints on degassing of magma: isothermal bubble growth during continuous decompression from high pressure. *Earth Planet. Sci. Lett.* **168** (1–2), 201–218. [https://doi.org/10.1016/S0012-821X\(99\)00051-5](https://doi.org/10.1016/S0012-821X(99)00051-5)

Gardner, J. E., Wadsworth, F. B., Carley, T. L., Llewellyn, E. W., Kusumaatmaja, H., and Sahagian, D., 2023. Bubble formation in magma. *Annu. Rev. Earth Planet. Sci.* **51**, 131–154. <https://doi.org/10.1146/>

[annurev-earth-031621-080308](#)

Giachetti, T., Druitt, T. H., Burgisser, A., Arbaret, L., and Galven, C., 2010. Bubble nucleation, growth and coalescence during the 1997 Vulcanian explosions of Soufrière Hills Volcano, Montserrat. *J. Volcanol. Geotherm. Res.* **193** (3–4), 215–231. <https://doi.org/10.1016/j.jvolgeores.2010.04.001>

Gonnermann, H. M., and Gardner, J. E., 2013. Homogeneous bubble nucleation in rhyolitic melt: Experiments and nonclassical theory. *Geochem. Geophys. Geosyst.* **14** (11), 4758–4773. <https://doi.org/10.1002/ggge.20281>

Guggenheim, E. A., 1952. Mixtures: the theory of the equilibrium properties of some simple classes of mixtures solutions and alloys. Clarendon Press.

Haasen, P., 1996. Physical metallurgy. Cambridge university press.

Hamilton, D. L., Burnham, C. W., and Osborn, E. F., 1964. The solubility of water and effects of oxygen fugacity and water content on crystallization in mafic magmas. *J. Petrol.* **5** (1), 21–39. <https://doi.org/10.1093/petrology/5.1.21>

Hirth, J. P., Pound, G. M., and St Pierre, G. R., 1970. Bubble nucleation. *Metall. Trans.* **1** (4), 939–945. <https://doi.org/10.1007/BF02811776>

Houghton, B. F., Carey, R. J., Cashman, K. V., Wilson, C. J., Hobden, B. J., and Hammer, J. E., 2010. Diverse patterns of ascent, degassing, and eruption of rhyolite magma during the 1.8 ka Taupo eruption, New Zealand:

evidence from clast vesicularity. *J. Volcanol. Geotherm. Res.* **195** (1), 31–47. <https://doi.org/10.1016/j.jvolgeores.2010.06.002>

Hummel, F., Marks, P. L., and Nowak, M., 2024. Preparatory experiments to investigate the vesicle formation of hydrous lower Laacher See phonolite at near liquidus conditions. EGU General Assembly 2024, Vienna, Austria, EGU24-19758. <https://doi.org/10.5194/egusphere-egu24-19758>

Iacono-Marziano, G., Schmidt, B. C., and Dolfi, D., 2007. Equilibrium and disequilibrium degassing of a phonolitic melt (Vesuvius AD 79 “white pumice”) simulated by decompression experiments. *J. Volcanol. Geotherm. Res.* **161** (3), 151–164. <https://doi.org/10.1016/j.jvolgeores.2006.12.001>

James, P. F., 1975. Liquid-phase separation in glass-forming systems. *J. Mater. Sci.* **10**, 1802–1825. <https://doi.org/10.1007/BF00554944>

Kakuda, Y., Uchida, E., and Imai, N., 1994. A new model of the excess Gibbs energy of mixing for a regular solution. *Proc. Jpn. Acad. B* **70** (10), 163–168. <https://doi.org/10.2183/pjab.70.163>

Kennedy, G. C., 1962. The upper three-phase region in the system $\text{SiO}_2\text{--H}_2\text{O}$. *Am. J. Sci.* **260**, 501–521. <https://doi.org/10.2475/AJS.260.7.501>

Lavallée, Y., Dingwell, D. B., Johnson, J. B., Cimorelli, C., Hornby, A. J., Kendrick, J. E., von Aulock, F. W., Kennedy, B. M., Andrews, B. J., Wadsworth, F. B., Rhodes, E., and Chigna, G., 2015. Thermal vesiculation

during volcanic eruptions. *Nature* **528** (7583), 544–547. <https://doi.org/10.1038/nature16153>

Le Gall, N., and Pichavant, M., 2016. Homogeneous bubble nucleation in H₂O- and H₂O–CO₂- bearing basaltic melts: Results of high temperature decompression experiments. *J. Volcanol. Geotherm. Res.* **327**, 604–621. <https://doi.org/10.1016/j.jvolgeores.2016.10.004>

Makhluף, A. R., Newton, R. C. and Manning, C. E., 2020. Experimental investigation of phase relations in the system NaAlSi₃O₈–H₂O at high temperatures and pressures: Liquidus relations, liquid-vapor mixing, and critical phenomena at deep crust-upper mantle conditions. *Contrib. Mineral. Petrol.* **175** (8), 76. <https://doi.org/10.1007/s00410-020-01711-2>

Marks, P. L., and Nowak M., 2024. Decoding the H₂O phase separation mechanism as the trigger for the explosive eruption of the Lower Laacher See phonolite. EGU General Assembly 2024, Vienna, Austria, EGU24-7723. <https://doi.org/10.5194/egusphere-egu24-7723>

Martel, C., and Schmidt, B. C., 2003. Decompression experiments as an insight into ascent rates of silicic magmas. *Contrib. Mineral. Petrol.* **144** (4), 397–415. <https://doi.org/10.1007/s00410-002-0404-3>

Marxer, H., Bellucci, P., and Nowak, M., 2015. Degassing of H₂O in a phonolitic melt: A closer look at decompression experiments. *J. Volcanol. Geotherm. Res.* **297**, 109–124. <https://doi.org/10.1016/j.jvolgeores.2014.11.017>

Moore, G., Vennemann, T., and Carmichael, I. S. E., 1998. An empirical

model for the solubility of H₂O in magmas to 3 kilobars. *Am. Mineral.* **83** (1–2), 36–42. <https://doi.org/10.2138/am-1998-1-203>

Mujin, M., and Nakamura, M., 2014. A nanolite record of eruption style transition. *Geology* **42** (7), 611–614. <https://doi.org/10.1130/G35553.1>

Murase, T., and McBirney, A. R., 1973. Properties of some common igneous rocks and their melts at high temperatures. *Geol. Soc. Am. Bull.* **84** (11), 3563–3592. [https://doi.org/10.1130/0016-7606\(1973\)84<3563:POSCIR>2.0.CO;2](https://doi.org/10.1130/0016-7606(1973)84<3563:POSCIR>2.0.CO;2)

Nguyen, C. T., Gonnermann, H. M., and Houghton, B. F., 2014. Explosive to effusive transition during the largest volcanic eruption of the 20th century (Novarupta 1912, Alaska). *Geology* **42** (8), 703–706. <https://doi.org/10.1130/G35593.1>

Nishiwaki, M., 2023. Chemical-thermodynamic explorations on the dissolution of water in magma: Breaking of the ideal mixing model and estimations of temperature change with decompression-induced vesiculation. Doctoral Dissertation, Kyushu University. https://catalog.lib.kyushu-u.ac.jp/opac_detail_md/?reqCode=frombib&lang=0&amode=MD823&opkey=B168673756684664&bibid=6787423&start=1&binfo_disp=0

Paillat, O., Elphick, S. C., and Brown, W. L., 1992. The solubility of water in NaAlSi₃O₈ melts: a re-examination of Ab–H₂O phase relationships and critical behaviour at high pressures. *Contrib. Mineral. Petrol.* **112**, 490–500. <https://doi.org/10.1007/BF00310780>

Preuss, O., Marxer, H., Ulmer, S., Wolf, J., and Nowak, M., 2016. Degassing of hydrous trachytic Campi Flegrei and phonolitic Vesuvius melts: Experimental limitations and chances to study homogeneous bubble nucleation. *Am. Mineral.* **101** (4), 859–875. <https://doi.org/10.2138/am-2016-5480>

Richet, P., Hovis, G., and Whittington, A., 2006. Water and magmas: Thermal effects of exsolution. *Earth Planet. Sci. Lett.* **241** (3–4), 972–977. <https://doi.org/10.1016/j.epsl.2005.10.015>

Richet, P., Hovis, G., Whittington, A., and Roux, J., 2004. Energetics of water dissolution in trachyte glasses and liquids. *Geochim. Cosmochim. Acta* **68** (24), 5151–5158. <https://doi.org/10.1016/j.gca.2004.05.050>

Sahagian, D., and Carley, T. L., 2020. Explosive volcanic eruptions and spinodal decomposition: A different approach to deciphering the tiny bubble paradox. *Geochem. Geophys. Geosyst.* **21** (6), e2019GC008898. <https://doi.org/10.1029/2019GC008898>

Shannon, R. D., 1976. Revised effective ionic radii and systematic studies of interatomic distances in halides and chalcogenides. *Acta Crystallogr. A: Found. Adv.* **32** (5), 751–767. <https://doi.org/10.1107/S0567739476001551>

Shea, T., 2017. Bubble nucleation in magmas: A dominantly heterogeneous process?. *J. Volcanol. Geotherm. Res.* **343**, 155–170. <https://doi.org/10.1016/j.jvolgeores.2017.06.025>

Shen, A. H., and Keppler, H., 1997. Direct observation of complete

miscibility in the albite–H₂O system. *Nature* **385** (6618), 710–712. <https://doi.org/10.1038/385710a0>

Shimozuru, D., Nakamuda, O., Seno, H., Noda, H., and Taneda, S., 1957. Mechanism of pumice formation. *Bull. Volcanol. Soc. Japan* **2**, 17–25.

Sowerby, J. R., and Keppler, H., 2002. The effect of fluorine, boron and excess sodium on the critical curve in the albite–H₂O system. *Contrib. Mineral. Petrol.* **143** (1), 32–37. <https://doi.org/10.1007/s00410-001-0334-5>

Sparks, R. S. J., 1978. The dynamics of bubble formation and growth in magmas: A review and analysis. *J. Volcanol. Geotherm. Res.* **3** (1–2), 1–37. [https://doi.org/10.1016/0377-0273\(78\)90002-1](https://doi.org/10.1016/0377-0273(78)90002-1)

Stolper, E., 1982a. Water in silicate glasses: An infrared spectroscopic study. *Contrib. Mineral. Petrol.* **81** (1), 1–7. <https://doi.org/10.1007/BF00371154>

Stolper, E., 1982b. The speciation of water in silicate melts. *Geochim. Cosmochim. Acta* **46** (12), 2609–2620. [https://doi.org/10.1016/0016-7037\(82\)90381-7](https://doi.org/10.1016/0016-7037(82)90381-7)

Tanaka, H., 1994. Critical dynamics and phase-separation kinetics in dynamically asymmetric binary fluids: New dynamic universality class for polymer mixtures or dynamic crossover?. *J. Chem. Phys.* **100** (7), 5323–5337. <https://doi.org/10.1063/1.467197>

Toramaru, A., 1989. Vesiculation process and bubble size distributions in ascending magmas with constant velocities. *J. Geophys. Res. Solid Earth*

94 (B12), 17523–17542. <https://doi.org/10.1029/JB094iB12p17523>

Toramaru, A., 1995. Numerical study of nucleation and growth of bubbles in viscous magmas. *J. Geophys. Res. Solid Earth* **100** (B2), 1913–1931. <https://doi.org/10.1029/94JB02775>

Toramaru, A., 2001. A numerical experiment of crystallization for a binary eutectic system with application to igneous textures. *J. Geophys. Res. Solid Earth* **106** (B3), 4037–4060. <https://doi.org/10.1029/2000JB900367>

Toramaru, A., 2006. BND (bubble number density) decompression rate meter for explosive volcanic eruptions. *J. Volcanol. Geotherm. Res.* **154** (3–4), 303–316. <https://doi.org/10.1016/j.jvolgeores.2006.03.027>

Toramaru, A., 2022. Vesiculation and crystallization of magma: Fundamentals of volcanic eruption process, conditions for magma vesiculation. Springer Singapore. <https://doi.org/10.1007/978-981-16-4209-8>

Toramaru, A., 2025. The theoretical basis for textural indices of eruption dynamics: review and new conceptual models. *Earth Planets Space* **77**, 27. <https://doi.org/10.1186/s40623-025-02146-4>

Toramaru, A., and Kichise, T., 2023. A new model of crystallization in magmas: Impact of pre-exponential factor of crystal nucleation rate on cooling rate exponent and log-linear crystal size distribution. *J. Geophys. Res. Solid Earth* **128** (10), e2023JB026481. <https://doi.org/10.1029/2023JB026481>

Verhoogen, J., 1951. Mechanism of ash formation. *Am. J. Sci.* **249**, 723–739.

Wang, Q. X., Zhou, D. Y., Li, W. C., and Ni, H. W., 2021. Spinodal decomposition of supercritical fluid forms melt network in a silicate–H₂O system. *Geochem. Perspect. Lett.* **18**, 22–26. <https://doi.org/10.7185/geochemlet.2119>

Zhang, Y., 1999. H₂O in rhyolitic glasses and melts: measurement, speciation, solubility, and diffusion. *Rev. Geophys.* **37** (4), 493–516. <https://doi.org/10.1029/1999RG900012>

CRedit authorship contribution statement

Mizuki Nishiwaki: Conceptualization, Methodology, Formal analysis, Investigation, Writing – Original Draft, Writing – Review & Editing, Visualization, Project administration, Funding acquisition.

Declaration of competing interest

The author declares that he has no known competing financial interests or personal relationships that could have appeared to influence the work reported in this paper.

Data availability

The author confirms that the data supporting the findings of this study are available within the article.

Table 1: Notation list.

Symbol	Unit	Definition
a_0	m	Average distance between water molecules in the melt
c	no unit	Water solubility in the melt (mole fraction)
$D_{\text{H}_2\text{O}}$	$\text{m}^2 \text{s}^{-1}$	Diffusivity of total water in the melt
g^{excess}	J mol^{-1}	Molar excess Gibbs energy for a regular solution
g^{ideal}	J mol^{-1}	Molar Gibbs energy of an ideal solution
g^{real}	J mol^{-1}	Molar Gibbs energy of mixing ($= g^{\text{ideal}} + g^{\text{excess}}$)
h^{excess}	J mol^{-1}	Molar excess enthalpy for a non-ideal solution
J	$\text{No m}^{-3} \text{s}^{-1}$	Nucleation rate
k_{B}	J K^{-1}	Boltzman's constant
n_0	No m^{-3}	Number of water molecules per unit melt volume
P	Pa	Pressure
P_{bi}	Pa	Pressure on the binodal curve (= binodal pressure)
P_{spi}	Pa	Pressure on the spinodal curve (= spinodal pressure)
P_{M}	Pa	Melt pressure
P_{SAT}	Pa	Water saturation pressure
P_{B}^*	Pa	Internal pressure of the critical bubble nucleus
R	$\text{J K}^{-1} \text{mol}^{-1}$	Gas constant
s^{excess}	$\text{J K}^{-1} \text{mol}^{-1}$	Molar excess entropy for a non-ideal solution (= 0 for a regular solution)
T	K	Temperature
$\bar{V}_{\text{H}_2\text{O}}$	$\text{m}^3 \text{mol}^{-1}$	Partial molar volume of water in the melt
w_{sym}	J mol^{-1}	Interaction parameter between two components for a symmetirc regular solution
$w_{\text{A,B}}$	J mol^{-1}	Interaction parameter between two components for an asymmetric regular solution
w_{ijk}	J mol^{-1}	Interaction parameter between three components for an asymmetirc regular solution
X	no unit	Symbolic notation for chemical composition
x	no unit	Mole fraction of one of the two components
$x_{\text{bi}}(P)$	no unit	The x that constitutes the binodal curve at pressure P
$x_{\text{spi}}(P)$	no unit	The x that constitutes the spinodal curve at pressure P
σ	N m^{-1}	“Microscopic” surface tension between the melt and homogeneous spherical bubble nucleus with a large curvature
σ_{∞}	N m^{-1}	“Macroscopic” surface tension at the flat interface between the melt and vapor